

Precise control of the filling stages in branched nanopores

C.T. Sousa¹, A. Apolinário¹, D.C. Leitão^{1,2}, A.M. Pereira¹, J. Ventura¹, J.P. Araújo^{1*}

¹ IFIMUP and IN-Institute of Nanoscience and Nanotechnology, Department of Physics and Astronomy, Faculdade de Ciências da Universidade do Porto, Rua do Campo Alegre, 678, 4169-007, Porto, Portugal

² INESC-MN and IN, Rua Alves Redol 9, 1000-029 Lisboa, Portugal

*jearaujo@fc.up.pt

Abstract

The filling of hierarchical branched porous anodic alumina (PAA) templates with magnetic and metallic nanowires using pulsed electrodeposition is here addressed in detail. We show that the electrodeposition potential (and current) reveals clear anomalies when each generation of branched pores created by steady-state or non-steady-state anodisation is completely filled, thus signalling clearly the growth stages. This allowed us to infer that each stage of PAA filling corresponds to a new hierarchical level of the branched structure. We show that the anomalies in the electrodeposition potential (current) were related with the change in porosity, and a linear relation between the electrodeposition potential and the template porosity during metal filling was established. Such a linear relation can be used as a new tool to easily determine the local porosity of anodic metal oxides, independently of the corresponding pore architecture. This work allows one to accomplish a precise control of the nanowires during their growth, opening a path to fill the several hierarchical levels of multiple branched pores with different materials, aiming for the production of multicomponent nanostructures.

1. Introduction

Metallic and magnetic nanowires (NWs) are a subject of relevant interest due to their promising application in a diversified set of fields, including resistive memory switching¹, plasmonic sensors², metamaterials³ and cell separation⁴. Among the various methods used for the NWs fabrication, template-assisted synthesis is an elegant physical-chemical approach and a reliable alternative to sophisticated nanopatterning methods¹⁻³. A successful example is porous anodic alumina (PAA), which has become widely used due to its easy fabrication method and the ability to tailor pore diameter and length at will. Besides self-organised pores, PAA also enables the assembly of multiple connected and hierarchically branched nanopores⁵. Moreover, the combination of PAA with electrochemical deposition is a cost-effective method to grow high-aspect-ratio NWs with uniform diameters, in a fast and well-controlled way.

To electrodeposit inside PAA, the alumina barrier-layer at the bottom of each nanopore (intrinsic to the anodisation process) must be removed or reduced. In the

direct current (DC) electrodeposition method, where a constant current (or potential) is used⁶, the PAA must be detached from the Al substrate and the barrier layer removed from the matrix structure, either by chemical wet etching or ion-milling processes. Afterwards, a metallic contact must be deposited on one side of the free-standing PAA, which acts as the working electrode. DC electrodeposition has proven to be a powerful technique, enabling substantial control of the NWs composition and crystallinity, even allowing compositional modulation along their length. Nevertheless, PAA filling using DC electrodeposition techniques shows major disadvantages for industrial applications due to the laborious template processing required, being only suitable for free-standing thick membranes ($>20\ \mu\text{m}$)⁷. To grow NWs of short lengths ($< 10\ \mu\text{m}$) one must use thin PAA and therefore retain the continuous barrier-layer. In this case, alternating current (AC) electrodeposition can be used in PAAs retaining the Al substrate, as long as the alumina barrier layer is reduced. The AC deposition procedure is simple and industrially scalable, and NWs of very small length can be produced. Nevertheless, the filling fraction of nanopores using AC deposition is generally low, a consequence of the high potentials applied. The latter also leads to hydrogen evolution that hinders deposition⁸.

To overcome this limitation, Nielsch and co-workers⁹ reported a pulsed electrodeposition method (PED) in PAA where the alumina barrier layer was thinned enough to enable electrodeposition using the Al substrate as the cathode. The reduction of the barrier-layer can be carried out using two strategies: non-steady-state and steady-state anodisation processes. In the non-steady-state anodisation, a reproducible tree-like branched structure, known as dendrites, is formed by exponentially decreasing the anodisation potential¹⁰. On the other hand, in the steady-state anodisation, the pores are rationally branched, taking into account the equal area model⁵. The main advantages of PED rely on its flexibility in adjusting the amplitude and time duration of the voltage pulses, offering the possibility to introduce a delay pulse to refresh the metallic ions concentration at the deposition interface, leading to an uniform growth of NWs. PED conditions have been optimised, and uniform high-aspect-ratio NWs of different materials such as Ni, Fe, Cu or Ag were reported^{8,11-13}. However, the potential behaviour during NWs growth, particularly during the filling of branched pores that exhibit a complex structure, is still under study^{9,13}. Understanding the relation between the ionic mass transport phenomena and the formation of NWs inside PAAs is therefore crucial to allow a more quantitative control of the nanoscale materials grown by this electrochemical method. Furthermore, the complex hierarchical levels of multiple branched NWs could be key to build components of nanoelectronics and nanoelectromechanical systems. Therefore, an accurate control of branched pore filling at each hierarchical level is of extreme importance.

In this work, the growth process of NWs by PED from stem to branched pores (increasing morphological complexity) was thoroughly investigated; the latter obtained either by a steady-state or non-steady-state anodisation. The potential behaviour during PED is analysed and correlated with the NWs growth stages using scanning electron microscopy images. Contrary to the three stages previously claimed, seven different growth stages were observed, four of them occurring during the branched structure

filling, each corresponding to a given hierarchical level. The electrodeposition voltage behaviour during NWs growth is explained by the effective electrodeposition area. Furthermore, a linear relation between PAA porosity and electrodeposition potential voltage is also established.

2. Experimental details

2.1. Fabrication of porous anodic alumina

PAA templates were prepared using a two-step anodisation process of 250 μm thick Al foils (99.997%) obtained from Alfa Aesar¹⁴. First, the Al surface was electropolished in an $\text{HClO}_4\text{:C}_2\text{H}_5\text{OH}$ solution (ratio 1:4) at 10° C with the application of 20 V for 2 min¹⁵. The first anodisation was carried out for 24 h at 2° C, (a) in 0.3 M $(\text{COOH})_2$ at 40 V, originating pores that were 35 nm in diameter (D_p) and with 105 nm of inter-pore distance (D_{int}); and (b) in a 0.1 M H_3PO_4 solution at 195 V, giving $D_p= 150$ nm and $D_{\text{int}}= 500$ nm. After the first anodisation process, a chemical dissolution of the resulting PAA was achieved by submerging the sample in an aqueous solution of H_3PO_4 (0.4 M) and $\text{H}_2\text{Cr}_2\text{O}_7$ (0.2 M) at 70° C for approximately 12 h. The second anodisation was performed under the same conditions as the first one but during different times, depending on the desired template thickness (a pore growth rate of 2.5 $\mu\text{m}/\text{h}$).

Following the second anodisation, pore branching with the consequent barrier-layer thinning was performed using two different routes: the non-steady-state anodisation and the steady-state anodisation. In the non-steady-state anodisation, which gives rise to tree-like branched pores¹⁶, the voltage was exponentially decreased from 40 V until reaching a final anodisation potential of 8 V, corresponding to a barrier layer thickness (δ_b) of 10 nm. In the case of the steady-state anodisation, the voltage was sequentially reduced by a $1/\sqrt{2}$ factor; two-, three-, and four-generations of Y-branched pores were then obtained by the reduction of the anodising voltage from 28.4 V to 10 V⁵.

2.2. Pulsed Electrodeposition

For electrodeposition, the PAA was used as a template, where the bottom Al substrate acted as the cathode and a Pt mesh as the counter electrode. Ni NWs were obtained from an aqueous solution containing 1 M $\text{NiSO}_4 \cdot 6\text{H}_2\text{O}$ and 0.2 M $\text{NiCl}_2 \cdot 6\text{H}_2\text{O}$ as the nickel source and 0.7 M H_3BO_3 serving as buffer¹⁷. The electrolyte temperature was kept constant at 40 °C during the electrodeposition process.

The PED was carried out by applying a modulated signal constituted by three pulses in the millisecond range (Fig. 1). First, a positive current pulse (t_i ; 8 ms) was applied to deposit the NWs ($j_{\text{app}}= 70 \text{ mAcm}^2$). In comparison to DC deposition, higher current densities are here applied at the moment of metal deposition⁹, which should increase the number of growth centres in each pore. Then, a shorter pulse (t_{ii} ; 2 ms) of negative

potential polarity ($V_{app} = 8$ V) is applied to discharge the barrier layer capacitance at the deposition interface. The amplitude of this voltage pulse corresponds to the final potential applied during the branched pore formation. Subsequently, a delay time (700 ms) at $V = 0$ V is applied to allow the recovery of the Ni^{2+} ion concentration at the deposition surface. This delay time is crucial to improve the homogeneity of the deposition and to limit hydrogen evolution⁹.

2.3. Characterisation

A Keithley 2400 Source Meter controlled by a homemade Labview program was used to perform both the anodisation and PED. The size and morphology of the fabricated nanostructures were analysed by Field Emission Scanning Electron Microscopy (FESEM) in a FEI Quanta 400 FEG SEM and by Transmission Electron Microscopy (TEM) in a LEO 906E Leica. Sample preparation steps for TEM measurements included PAA dissolution with H_3PO_4 (0.4 M) and magnetic separation, followed by a thorough washing in bi-deionised water and final re-suspension in ethanol (0.5 mL). The porosity (P) for all dendrite generations and stem pores was determined with the given equation¹⁸:

$$P = \frac{2\pi}{\sqrt{3}} \left[\frac{D_p/2}{D_{int}} \right]^2 \quad (1)$$

where D_p and D_{int} are the pore diameter and the inter-pore distance, respectively. These values were extracted from the SEM and TEM images using an open source software for image analysis¹⁹. The porosity was then determined using Eq. (1) in samples anodised in H_3PO_4 due to their larger dimensions that allow for easier and more accurate measurement.

3. Results and discussion

3.1. PAA templates with multiple generations of branched pores

The fabrication of Ni NWs was performed by PED in PAA templates with branched pores. Figures 2(a) and (c) show the applied voltage (V) to form the branched pores in non-steady-state and steady-state anodisation conditions, respectively, and the consequent thinning of δ_b ^{5,20}. Generally, such V decrease influences the porous structure in two ways: it thins the barrier layer and induces a change in the porosity (fractional 2-D surface area occupied by the pores, given by Eq. 1), leading to a branched structure^{5,21}. Upon each V decrease step, a new state is achieved with a corresponding porosity, anodisation current [$j_{anod}(t)$], and δ_b ^{22,23}.

Figures 2(b) and (d) show the typical time dependence of $j_{anod}(t)$ during the formation of multiple generations of branched pores in the non-steady-state and steady-state anodisation conditions, respectively. In the non-steady-state regime, each voltage reduction step was followed by a sudden decrease in the measured $j_{anod}(t)$. This stage is

readily followed by a subsequent increase towards an equilibrium $j_{anod}(t)$ value, indicating the onset of a new balance between oxide formation and dissolution [inset of Fig. 2(b)]. However, before $j_{anod}(t)$ becomes stable, $V(t)$ is again reduced, and a new non-steady-state anodisation process occurs.

In the steady-state anodisation, the voltage was sequentially reduced in $1/\sqrt{2}$ steps [Fig.2(c)]. Each reduction in the applied potential was followed by low $j_{anod}(t)$ values due to the small electric field across the alumina barrier-layer. However, after few minutes, $j_{anod}(t)$ began to increase, reaching a new stable value when the balance between the field assisted dissolution and formation of alumina was attained. In this case, we used extended anodization times (100 min for each generation of dendrites), allowing the pore to achieve a stable growth rate, thus translating into a more uniform D_p . Only after $j_{anod}(t)$ becomes stable, is $V(t)$ again reduced and a new pore generation created. These successive steps in steady-state anodisation, as well as the exponential $V(t)$ reduction in non-steady-state anodisation, lead to the hierarchical branched structure shown in Fig. 3.

Notice that the dendrites formed during the non-steady-state anodisation are expected to be different from branched nanopores obtained in steady-state conditions¹⁰. In the latter an n -branched structure is obtained when one applies a voltage according to^{24,25}:

$$V_{Gn} = (1/\sqrt{n}) \cdot V_S, \quad (2)$$

where V_{Gn} is the potential necessary to nucleate n -pores and V_S is the potential used to generate the stem pores. This relation is based on the simplified equal area model, in which the area of the stem pore matches the area of the n generated ones²⁴. On the other hand, in the non-steady-state anodisation, pore growth resembles the development of a tree or root in nature, being also reminiscent of electrical treeing in insulator materials under applied voltages^{21,26}.

Monitoring $j_{anod}(t)$ during dendrites formation allow us to better understand the pore formation in the non-steady-state anodisation process. As shown in Fig. 2(b), $j_{anod}(t)$ displays two asymptotic regimes. In the first, lasting up to 8 min (which corresponds to applied potentials from 40 to 28.3 V), $j_{anod}(t)$ has a strong decrease. For this regime, one observes a δ_p and D_p decrease of the stem pores with the applied potential, originating from narrow stem pores. Figure 3(a) shows a TEM image of Ni NWs grown in PAA stem pores with $D_p = 35$ nm and non-steady-state branched pores structures at the bottom. Here, one can observe that after the $V(t)$ anodisation reduction, the stem pores continue to grow with smaller D_p (27 nm), and just before branching, D_p increases again (narrow NWs). In the NW TEM picture [Fig. 3(a)] one can also see a clear decrease of the NW diameter from 35 nm to 27 nm before increasing again to 42 nm just before the bifurcation in two branched pores.

This effect leads to the PAA porosity shown in Table 1. When $V(t)$ decreases below a critical value, the corresponding electric field is no longer compatible with the current D_p , thus creating instabilities that result in a higher alumina dissolution-rate when compared to the formation rate. Therefore, D_p increases while D_{int} remains constant, leading to an increase in the porosity (Table 1), as one observes in Fig. 3(b). Below 28.3

V , a smaller $j_{anod}(t)$ slope is visible as a new equilibrium state is established with a specific pore density (porosity), creating the first generation (G1) of n-branched pores [Figs. 3(a) and (b)]. This anodisation voltage correlates with the applied potential during the second anodisation by a factor of $1/\sqrt{2}$, showing that each stem pore is divided in two new pores, as expected, taking into account the equal area model^{24,26}. Afterwards, the 2nd (G2), 3rd (G3) and 4th (G4) generations of n-branched (G_n) pores are obtained by further reducing the anodisation voltage down to 8 V [Fig. 3(b)]. Notice that for each dendrite generation, the process described above for the G1 formation was observed, with specific D_p and porosities. In fact, only with a small dispersion regarding the starting point of the consecutively branched pore is observed (G2, G3 and G4) originated from local inhomogeneities at the electrolyte/oxide/metal interfaces [Fig. 3(b)]. Table 1 shows the D_p , length (L) and porosity for all dendrite generation and stem pores, determined using TEM and SEM images of samples anodised in H_3PO_4 due to their larger dimensions, which allow easier and more accurate measurement.

3.2. PED stages in branched pores

As shown in Fig. 4, both the deposition potential (V_{dep}) for NW growth at constant j_{app} (t_I in Fig. 1) and the current density after the discharge pulse at V_{app} (t_{II} in Fig. 1) were measured during the PED process and for each pulse.

In the literature, the PED process in PAA templates after the alumina barrier-layer thinning is usually divided in three different regions^{11,13}. The first is identified by an increase in V_{dep} associated with the branched structure filling; then, a region of almost constant V_{dep} follows, attributed to the growth of the NWs inside the main cylindrical pores; finally, a decrease in V_{dep} appears when the NWs start to come out of the pores. However, our results clearly show that sub-steps can be established for PED in PAA with branched pores obtained both in non-steady-state and steady-state anodisation [Figs. 4(a) and (c), respectively]. Seven stages during the growth process were identified, enabling a more accurate control over the stage of pore filling for such complex structures as schematized in Fig. 4(e).

Figure 4(a) shows V_{dep} during filling of the PAA with branched pores obtained in non-steady-state anodisation. First, V_{dep} increases from 8.4 V to 9.1 V (up to $t = 4$ s, where dV_{dep}/dt has the first local minimum), here defined as stage I and II corresponding to G4 and G3 dendrites filling. Stage III then extends up to $t = 23$ s with the progress of the Ni electrodeposition along the G2 dendrites, as also observed in the SEM image [Fig. 5(a)]. The G1 dendrites filling occur after 51 s and lead to a potential increase up to 12.8 V [Stage IV; Fig. 5(b)]. After completely filling the dendrites, a small decrease in the potential is associated with the filling of the narrow pores (Stage V). Then, the profile of the $V(t)$ curve in stage VI [Fig. 5(c)] is responsible for filling 1 μm in length in 6 minutes, corresponding to an electrodeposition rate of 4 nm/s. Finally, when the NWs start to emerge from the pores [stage VII; Fig. 5(d)], a sudden decrease in V_{dep} and increase in noise is observed.

The stages of dendrites filling are more evident in the dV_{dep}/dt presented in Figs. 4(b) and (d). The G1 filling corresponds to the rapid site nucleation during the two first PED pulses and is therefore indistinguishable from the G2 filling. However, for each branched pore generation, the pore filling starts at a minimum value of dV_{dep}/dt which corresponds to a larger pore area than the previous generations. Then the potential reaches a maximum value, where D_p is minimum. Interestingly, before moving to a new pore generation, D_p increases again, which leads to a new decrease in the dV_{dep}/dt of each stage. This is in complete accordance with the measured D_p values along each dendrite generation (Table 1).

For the case of PAA with branched pores obtained in steady-state anodisation, V_{dep} presents clear levels during template filling, each attributed to the filling of distinct generation of branched pores [Fig. 4(c)]. However, the overall increase in V_{dep} during the branched pores filling is smaller (3.1 V), which is a consequence of the lower variation in D_p along the pores. The electrodeposition time for branched pores filling is also longer for the steady-state due to their increased length [Fig. 3(c)]. Furthermore, stage V (narrow-like pore filling) is only observed in PAA with branched pores obtained in non-steady-state anodisation due to the continuous $V(t)$ decrease between 40 V and 28.3 V.

During the PED process, the Ni ions from the solution are reduced at the barrier-layer/electrolyte interface, nucleating at the bottom of the branched pores. The material begins to fill the G_n ($1 \leq n \leq 4$) dendrites with characteristic D_p , D_{int} and porosities [Fig. 3(b); Table 1]. In the stem pores and in each pore generation, D_{int} remains constant, and D_p is proportional to the applied electric field. On the other hand, at the transition from the stem pore to G_1 and at the branching points between different pore generations, a new D_{int} value is attained. The stem pore growth in the self-organised regime with $D_p = 35$ nm and $D_{\text{int}} = 105$ nm originates a porosity of 10% and presents the same alumina formation/dissolution rate at the pore bottom¹⁸. When the anodisation potential decreases, D_p first diminishes until a value where the weak electric field leads to a smaller dissociation rate of water, inducing a higher rate of alumina dissolution than formation and thus an increase of D_p [inset of Fig. 3(a)]²². Then, when the anodisation potential reaches a value corresponding to a new stable D_{int} , pore branching occurs, creating two new pores with specific D_p and D_{int} [inset of Fig. 3(a)]. For the electrolyte used, the anodisation potential is far from the one corresponding to the self-organised regime, leading to a modulation of D_p and a strong deviation of the porosity from 10% (see Table 1). Moreover, this modulation of the porosity along several generations of branched pores has a direct impact on the effective electrodeposition area during NWs growth. The almost constant V_{dep} measured during the filling of the uniform pore region (stage VI; section with uniform porosity) shows that V_{dep} is rather insensitive to the NW length. Therefore, the V_{dep} increase during the dendrites filling reflects mainly the changes in the effective electrodeposition area due to the different local porosity. Finally, stage VII results from the rapid increase of the deposition area, which occurs when the pores are completely filled with metal. Here, the electrodeposits begin to form hemispherical caps over the top of each NW that eventually coalesce into a metallic thin

film at the surface [Fig. 5(d)]. The formation of these structures originates from a V_{dep} decrease.

Figure 4 also shows that the current measured after each discharge pulse in the PED process (j_{dis}) in non-steady-state [Fig. 4(a)] and steady-state [Fig. 4(c)]. Similarly to V_{dep} , different stages in the j_{dis} curve are identified. In Stages I and II, j_{dis} reaches its maximum value. Then, in Stage III, j_{dis} decreases abruptly down to $5 \mu\text{A}/\text{cm}^2$, reaching Stage IV where it continues to decrease, although with a smaller slope. Then, a noticeably constant j_{dis} value is visible (Stage VI), increasing again at ≈ 400 s, corresponding to Stage VII. For the steady state anodization, a similar tendency as the one observed for V_{dep} is present, with clear and distinct levels, decreasing in intensity towards the minimum value close to $5 \mu\text{A}/\text{cm}^2$.

The j_{dis} measured after the discharge pulses (t_{II}) in the PED process also translates the mechanisms of pore filling. Different stages exist that can be related to the different phases of NW growth in the branched pores, as described above. Notice that the PAA template can be characterised in terms of an equivalent circuit model with several electrochemical impedance contributions²⁷. In stages I to IV, the j_{dis} decrease is associated with the decrease of the effective metallic electrodeposition area. In stage VI, the growth of the homogeneous NWs occurs with the smaller discharge current value. Finally, j_{dis} increases in stage VII, when the NWs come out of the PAA. Like V_{dep} , j_{dis} also evidences the porosity modulation along the several generations of PAA pores.

3.3. Porosity rule in branched PAA

Figure 6 shows V_{dep} as a function of the porosity along the length of PAA with branched pores. V_{dep} was taken at maximum and minimum dV_{dep}/dt , where the porosity was also measured (Table 1). A remarkable linear dependence was observed, evidencing that the V_{dep} increase in the first four PED stages is due to the decrease of the effective electrodeposited area, which in turn reflects the decrease of the PAA porosity from 32% to 10%^{18,22}.

The relation found between porosity and V_{dep} can also be used to easily determine the local porosity of a porous anodic metal oxide film, independently of the corresponding pore architecture. Based only on the potential needed to fill the pores using electrodeposition:

$$P_{\text{Gn}} = \alpha (V_{\text{dep}}^{\text{Gn}} - V_{\text{dep}}^{\text{S}}) + 10\%$$

where $V_{\text{dep}}^{\text{S}}$ is the electrodeposition potential for filling stem pores and $V_{\text{dep}}^{\text{Gn}}$ to fill G_n dendrites generation, and α is a constant associated with the nature of the electrodeposited material (for Ni, $\alpha = 5.6$), one is able to infer directly the D_p/D_{int} ratio without resorting to imaging techniques.

4. Conclusions

This work presents a detailed study of the stages of PED for the growth of NWs in PAA with branched pores. Seven different growth stages were observed, with four of them occurring during the branched structure filling, each corresponding to a given hierarchical level. The close monitoring of the distinct stages of PED allows a precise and effective control of the PAA filling from the stem pores to multiple branched structures, enabling one to directly infer on the template porosity, i.e., D_p and D_{int} . A linear dependence between the electrodeposition potential (V_{dep}) and the PAA porosity during template filling was established, yielding an additional degree to control PAA filling, including templates with branched pores formed in steady-state and non-steady-state anodisation. We found that the PAA porosity is the crucial parameter driving the behaviour of V_{dep} during the filling of complex branched structures. The linear dependence between V_{dep} and porosity can now be applied to the pore filling of other anodic metal oxides with Ni NWs or other metallic materials.

This work allows one to accomplish further control on the homogeneity and length of the NWs, opening a window to selectively fill the several hierarchical levels of multiple branched pores with different materials and providing a powerful approach to produce multicomponent nanostructures for a large range of applications.

Acknowledgements

Work supported in part by projects NANO/NMED-SD/0140/2007 and FEDER/POCTI/n2-155/94. Funding from FCT through the Associated Laboratory-IN is acknowledged. C.T. Sousa, D.C. Leitaó, and A.M. Pereira are thankful to FCT for grants SFRH/BD/38290/2007, SFRH/BPD/72359/2010 and SFRH/BPD/63150/2009, respectively. A. Apolinário acknowledges the financial support under project PTDC/EQU-EQU/107990/2008. J. Ventura acknowledges financial support through FSE/POPH. J.P. Araujo also thanks Fundacao Gulbenkian for its financial support within the "Programa Gulbenkian de Estimulo a Investigacao Cientifica".

References

- (1) Oka, K.; Yanagida, T.; Nagashima, K.; Kawai, T.; Kim, J. S.; Park, B. H. *Journal of the American Chemical Society* **2010**, *132*, 6634.
- (2) Kabashin, A. V.; Evans, P.; Pastkovsky, S.; Hendren, W.; Wurtz, G. A.; Atkinson, R.; Pollard, R.; Podolskiy, V. A.; Zayats, A. V. *Nature Materials* **2009**, *8*, 867.
- (3) Yao, J.; Liu, Z. W.; Liu, Y. M.; Wang, Y.; Sun, C.; Bartal, G.; Stacy, A. M.; Zhang, X. *Science* **2008**, *321*, 930.
- (4) Song, M. M.; Song, W. J.; Bi, H.; Wang, J.; Wu, W. L.; Sun, J.; Yu, M. *Biomaterials* **2010**, *31*, 1509.

- (5) Meng, G. W.; Jung, Y. J.; Cao, A. Y.; Vajtai, R.; Ajayan, P. M. *Proceedings of the National Academy of Sciences of the United States of America***2005**, *102*, 7074.
- (6) Whitney, T. M.; Jiang, J. S.; Searson, P. C.; Chien, C. L. *Science***1993**, *261*, 1316.
- (7) Wu, C. G.; Lin, H. L.; Shau, N. L. *Journal of Solid State Electrochemistry***2006**, *10*, 198.
- (8) Gerein, N. J.; Haber, J. A. *Journal of Physical Chemistry B***2005**, *109*, 17372.
- (9) Nielsch, K.; Muller, F.; Li, A. P.; Gosele, U. *Advanced Materials***2000**, *12*, 582.
- (10) Cheng, W. L.; Steinhart, M.; Gosele, U.; Wehrspohn, R. B. *J. Mater. Chem.***2007**, *17*, 3493.
- (11) Leitao, D. C.; Ventura, J.; Sousa, C. T.; Pereira, A. M.; Sousa, J. B.; Vazquez, M.; Araujo, J. P. *Physical Review B***2011**, *84*, 014410.
- (12) Sun, L.; Zhang, L. D.; Liang, C. H.; Yuan, Z. G.; Zhang, Y.; Xu, W.; Zhang, J. X.; Chen, Y. Z. *J. Mater. Chem.***2011**, *21*, 5877.
- (13) Sauer, G.; Brehm, G.; Schneider, S.; Nielsch, K.; Wehrspohn, R. B.; Choi, J.; Hofmeister, H.; Gosele, U. *Journal of Applied Physics***2002**, *91*, 3243.
- (14) Masuda, H.; Fukuda, K. *Science***1995**, *268*, 1466.
- (15) Leitao, D. C.; Apolinario, A.; Sousa, C. T.; Ventura, J.; Sousa, J. B.; Vazquez, M.; Araujo, J. P. *Journal of Physical Chemistry C***2011**, *115*, 8567.
- (16) Sousa, C. T.; Leitao, D. C.; Proenca, M. P.; Apolinario, A.; Correia, J. G.; Ventura, J.; Araujo, J. P. *Nanotechnology***2011**, *22*.
- (17) Schlesinger, M.; Paunovic, M. *Modern Electroplating*; Wiley Inter-Science, 2000.
- (18) Nielsch, K.; Choi, J.; Schwirn, K.; Wehrspohn, R. B.; Gosele, U. *Nano Letters***2002**, *2*, 677.
- (19) Rasband, W. S.; US National Institutes of Health <http://rsb.info.nih.gov/ij/>; Bethesda, Maryland, 1997–2005
- (20) Marquardt, B.; Eude, L.; Gowtham, M.; Cho, G.; Jeong, H. J.; Chatelet, M.; Cojocaru, C. S.; Kim, B. S.; Pribat, D. *Nanotechnology***2008**, *19*.
- (21) Furneaux, R. C.; Rigby, W. R.; Davidson, A. P. *Nature***1989**, *337*, 147.
- (22) Ono, S.; Saito, M.; Ishiguro, M.; Asoh, H. *Journal of the Electrochemical Society***2004**, *151*, B473.
- (23) Su, Z. X.; Zhou, W. Z. *Advanced Materials***2008**, *20*, 3663.
- (24) Thompson, G. E.; Wood, G. C. *Nature***1981**, *290*, 230.
- (25) Shuoshuo, C.; Zhiyuan, L.; Xing, H.; Yi, L. *J. Mater. Chem.***2009**, *19*, 5717.
- (26) Hanaoka, R.; Takata, S.; Nakagami, Y. *Ieee Transactions on Dielectrics and Electrical Insulation***2004**, *11*, 939.
- (27) Jagminiene, A.; Valincius, G.; Riaukaite, A.; Jagminas, A. *Journal of Crystal Growth***2005**, *274*, 622.

Figure 1. Current and voltage pulses applied during PED. First, a positive current pulse is applied (t_I) to deposit the metallic material. Secondly, a limited potential pulse (t_{II}) is used to discharge the capacitor constituted by the alumina barrier layer, and finally, a long delay pulse (t_{III}) to avoid the depletion of the metallic ions near the deposition interface.

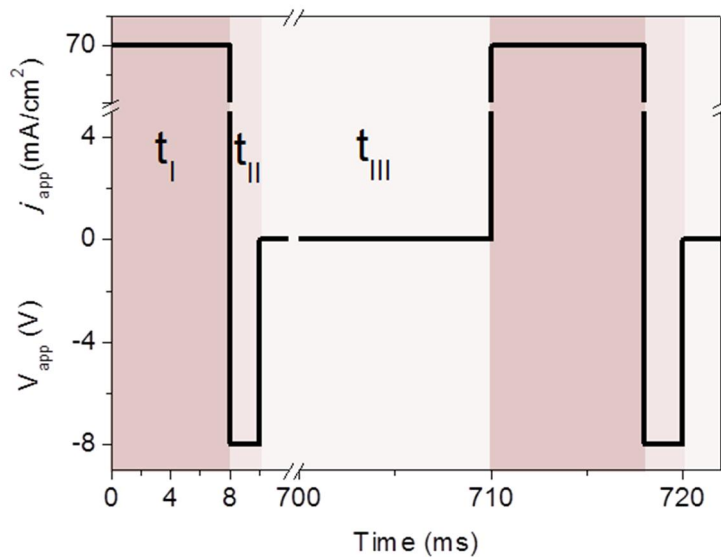


Figure 2. (a) $V(t)$ and (b) $j_{anod}(t)$ recorded during the non-steady-state-anodisation and corresponding magnified views (insets). (c) $V(t)$ and (d) $j_{anod}(t)$ recorded during the steady-state-anodisation.

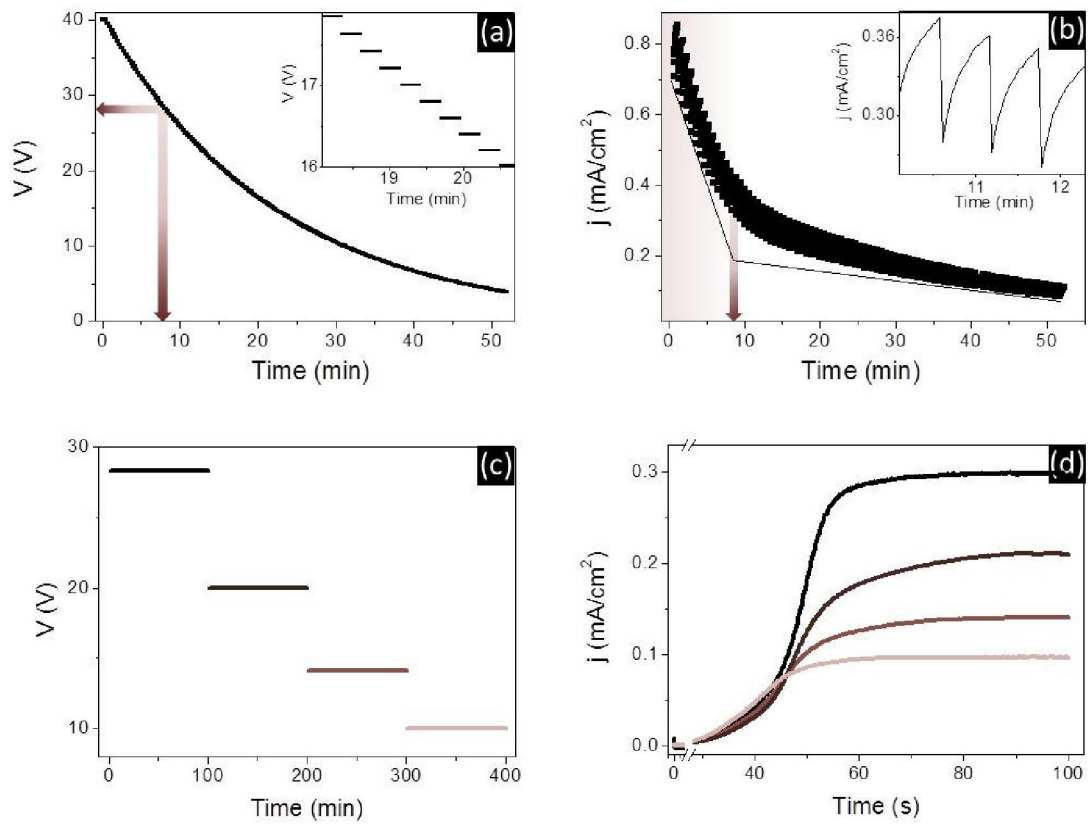


Figure 3. NWs grown on non-steady state anodised PAA (inset: scheme of D_p and D_{int} profile in two pores): (a) TEM image of a Ni NW ($D_p = 35$ nm) with dendrites and (b) SEM image of Ni NWs with $D_p = 200$ nm and the different dendrite generations. NWs grown on steady-state anodised PAA: (c) cross sectional SEM image of Ni NWs in PAA ($D_p = 35$ nm) with branched pores.

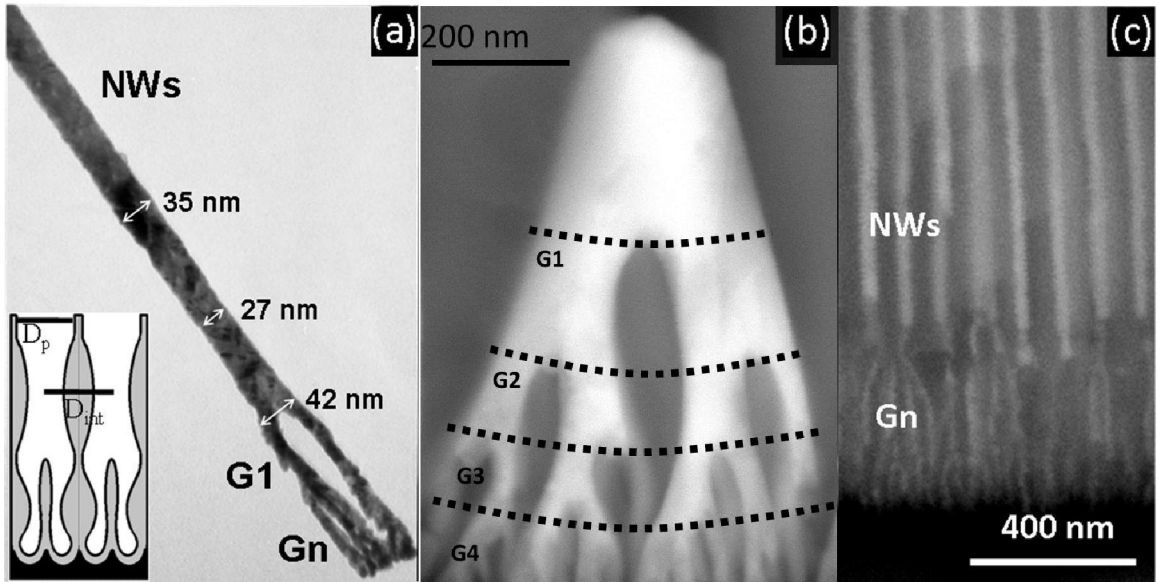


Figure 4. Current density and potential behaviour for PED inside PAA with dendrites grown by (a) non-steady-state anodisation and (c) steady-state-anodisation; (b), (d) corresponding numerical dV_{dep}/dt that evidences the several generations of dendrite filling; and (e) scheme of dendrites and pore filling for each step.

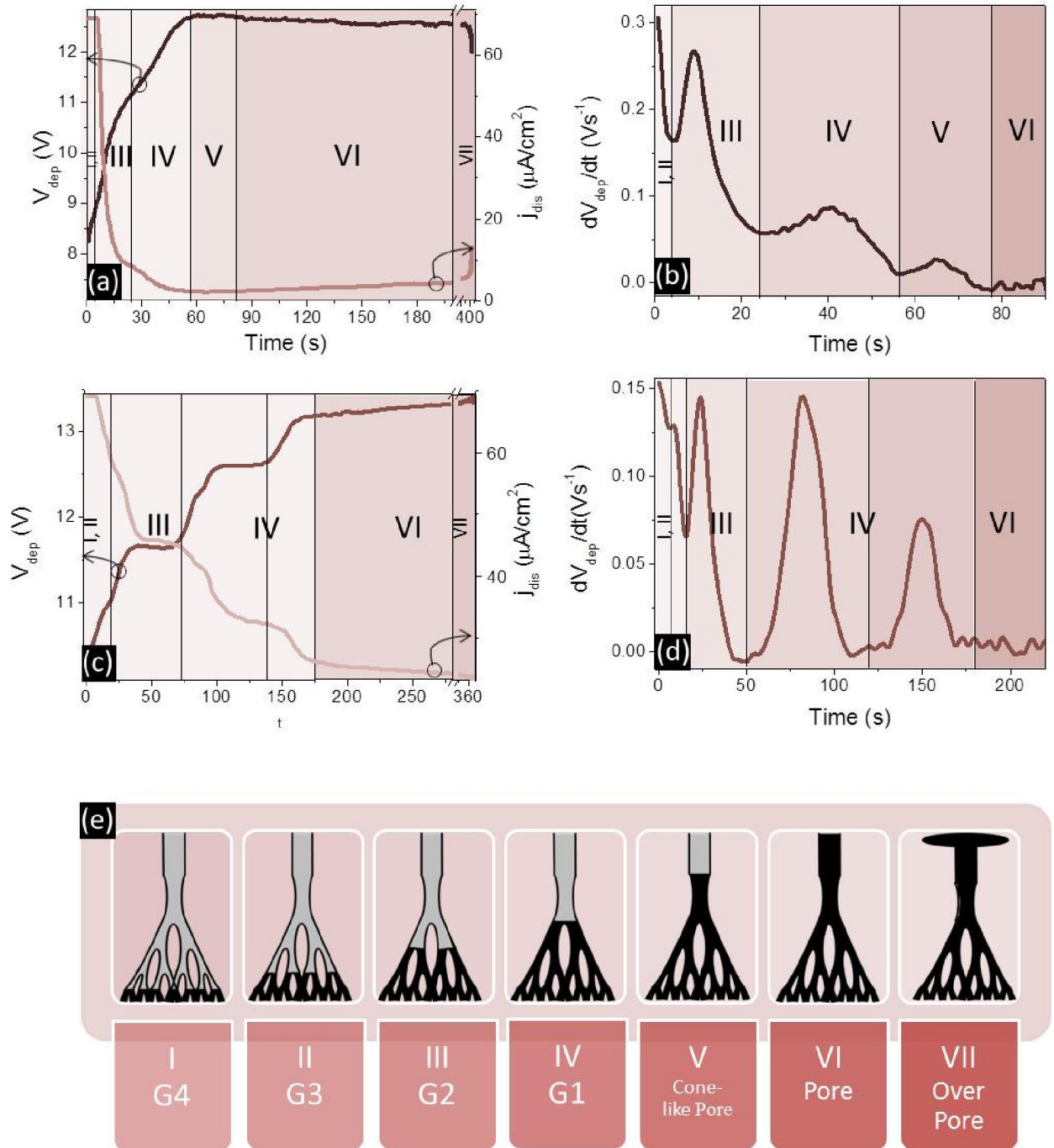


Figure 5. SEM images of filled PAA in the four stages corresponding to the PED process: (a) stage III, $t = 23$ s; (b) stage IV, $t = 51$ s; (c) stage VI, $t = 400$ s; (d) stage VII.

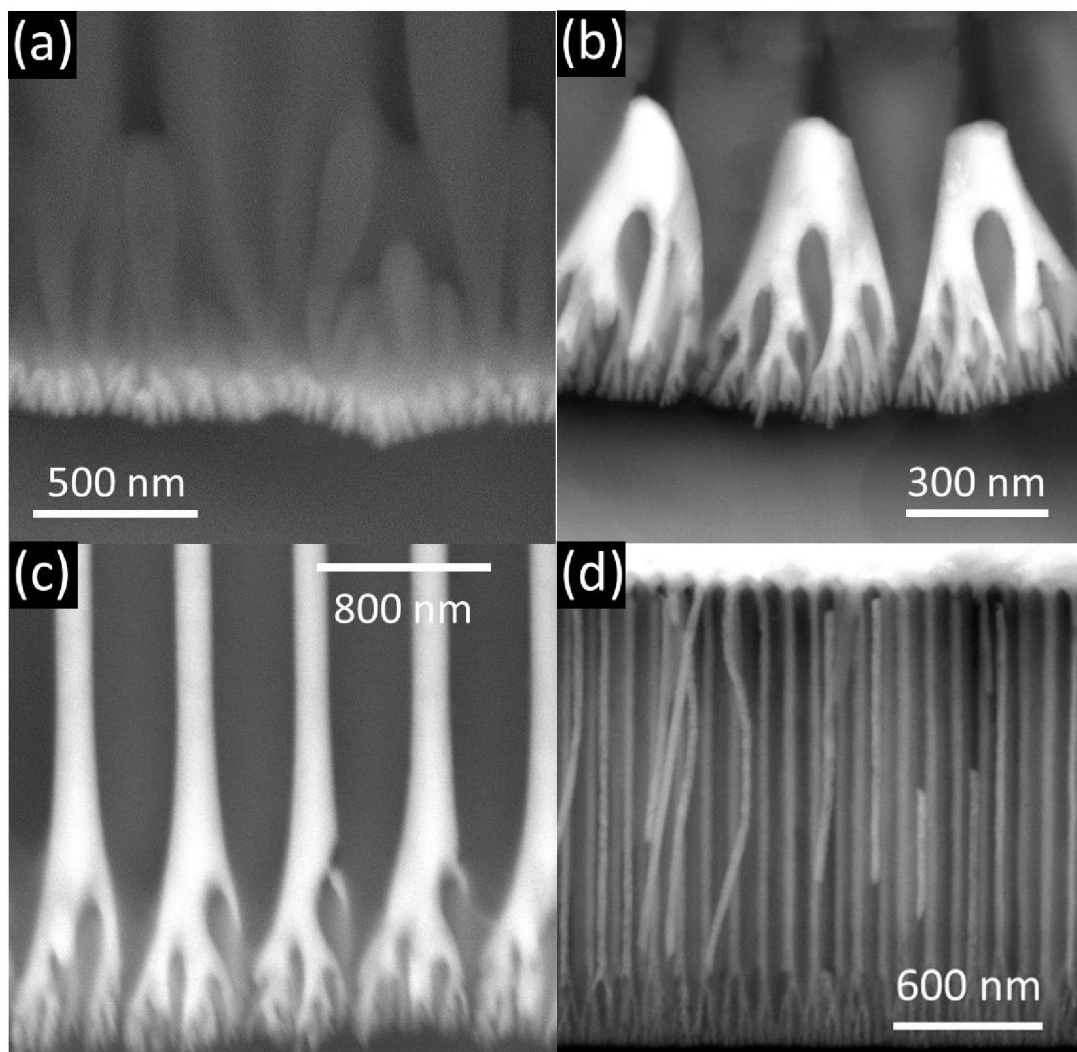


Figure 6. V_{dep} dependence on the PAA porosity.

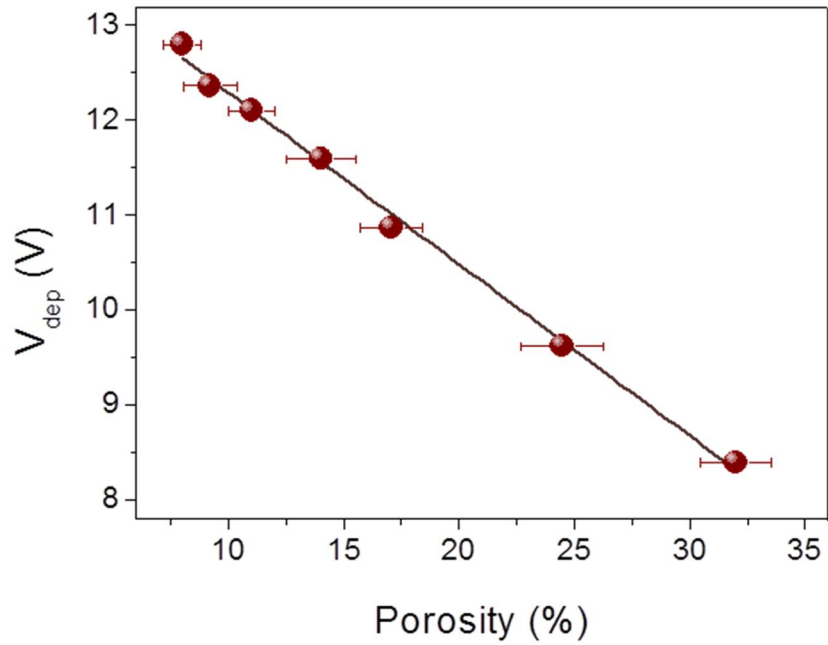


Table 1. D_p , L and porosity in each pore generation.

	D_p (nm)	L (nm)	P (%)
NW	150	1000	10
Cone-like	130	153	8
NW	145		9
G1	70	126	9
	80		10
G2	40	90	14
	50		17
G3	25	90	25
	30		32